

Pedestal properties of H-modes with negative triangularity using the EPED-CH model

A. Merle¹, O.Sauter¹, S.Yu. Medvedev^{2,3}

¹ École Polytechnique Fédérale de Lausanne (EPFL), Swiss Plasma Center (SPC), CH-1015 Lausanne, Switzerland

² Keldysh Institute, Russian Academy of Sciences, Moscow, Russia

³ National Research Nuclear University MEPhI, Moscow, Russia

E-mail: antoine.merle@epfl.ch

Abstract.

The EPED model has been designed to predict the pedestal height and width from a minimal set of parameters and using the stability of the pedestal region for global MHD peeling-ballooning (P-B) modes as well as local Kinetic Ballooning Modes (KBMs). This approach has been validated for type-I ELMy H-modes and Quiescent H-modes (QH) but can also be used for other types of H-modes where it usually sets an upper limit on the achievable pedestal height.

Using the recently developed EPED-like model called EPED-CH and based on the equilibrium codes CHEASE and CAXE and the MHD stability code KINX, we investigate in this work the effect of negative triangularity on the pedestal structure. Our simulation results confirm the experimental results from TCV where a reduction of the pedestal height was observed when going from positive to negative top triangularity. This was interpreted as a degradation of the peeling-ballooning stability due to the closed access to the second stability region for ballooning modes in the case of negative triangularity. This effect is further enhanced by the coupling to the KBM stability criterion in EPED simulations.

The novel concept of the Negative Triangularity Tokamak (a DEMO-sized machine) is also investigated. Again a strong reduction of the pedestal height and width is observed going from positive to negative triangularity for up-down symmetric equilibria. The pedestal height is also reduced going to more up-down asymmetric cases. The beneficial effect of the global β value on the pedestal height, which is linked to the second stability access, is strongly reduced for negative triangularity.

Keywords: Plasma instabilities, Edge localized modes, Plasma transport properties

Submitted to: *Plasma Phys. Control. Fusion*

1. Introduction

The heat exhaust problem becomes more and more important as tokamaks are evolving to the reactor scale. Namely, the divertor plates must be able to withstand large heat fluxes, especially during transient events such as Edge Localized Modes (ELMs). The standard approach optimises first the core performance. This has led to tokamaks with positive triangularity which maximise the pedestal height by providing good stability properties. However higher pedestals often lead to larger ELM losses and transient heat fluxes that require mitigation. The Negative Triangularity Tokamak (NTT) is a reactor concept which uses another approach with the heat exhaust problem as the primary concern [1, 2].

By moving the X-point to the low-field side (LFS) and thus to larger values of R , the divertor wetted area is larger leading to a geometrical reduction of the peak heat flux. In addition the magnetic field amplitude at the divertor coils is smaller allowing for more innovative divertor concepts like the snowflake divertor which can help further reduce the heat flux. L-mode experiments on TCV with negative triangularity have shown an improvement by a factor of two in the electron energy confinement compared to mirrored positive triangularity discharges in low collisionality conditions [3], the ion energy confinement also improved and as a result the global energy confinement time was nearly doubled. This improvement was not recovered in high collisionality conditions such as H-mode so far. However, it was shown in TCV H-mode experiments that ELMs are becoming more frequent and carry less energy when going from positive to negative triangularity [4]. However this correlates with a reduction of the pedestal height p_{ped} and global confinement. On the negative side, plasmas are found to be more vertically unstable [5] and a new study using the GBS code has found that the scrape-off layer width is smaller [6].

The usual figure of merit when considering ELM losses is the value of the ELM energy loss ΔW_{ELM} normalised to the pedestal stored energy $W_{ped} = (3/2)p_{ped}V$ where V is the plasma volume. This quantity has been recognised to be similar across devices when the plasma conditions are similar [7]. However certain experimental studies have found that reduced ΔW_{ELM} do not necessarily translate into reduced heat fluxes as the ELM wetted area can also be reduced in that case [8]. The EPED model [9, 10] has been successful at predicting the pedestal structure, namely its height p_{ped} and width Δ , for tokamaks operating in type-I ELMy H-modes and Quiescent H-modes (QH) [11]. For other regimes, such as type-III ELMy, ELM-mitigated or ELM-suppressed regimes, the experimental pedestal height generally lies below the EPED prediction. The motivation for this article is to study how adopting negative triangularity as part of the tokamak design can help reduce the transient heat loads due to ELMs. To this end we use the EPED model to study the influence of triangularity and other plasma parameters on p_{ped} and W_{ped} using the NTT as the base case, and we make the assumption that lower W_{ped} means lower ΔW_{ELM} .

After this introduction, section 2 shortly describes the EPED model before introducing EPED-CH, a new implementation of the EPED model (in its EPED1 version) using the SPC suite of codes in section 3. A prediction for the Negative Triangularity Tokamak pedestal height is formulated in section 4 which then discusses the effect of negative triangularity on the pedestal structure. Finally section 5 presents a discussion of the results presented in this paper.

2. The EPED Model

The EPED model [9, 10] relies on the hypothesis that the pedestal evolution is limited by two constraints. The first constraint is the crossing of the peeling-ballooning (P-B) limit which triggers type-I ELMs. This is a global constraint on the pedestal structure. The second constraint is the onset of small-scale turbulence in the pedestal region, assumed to be driven by kinetic ballooning modes (KBM), although more local in nature this can also be expressed as a global constraint on the pedestal structure.

The peeling-ballooning constraint is generally computed using a linear ideal MHD code (such as ELITE for the original EPED model) which computes for a given equilibrium the ideal MHD growth rate as a function of the toroidal mode number n . Diamagnetic stabilisation of high- n modes is usually included using simplified analytic theory [12] or fits to two-fluid calculations [10]. The radially integrated KBM constraint, in the EPED1 version, calculates a scaling of the pedestal width in normalized poloidal flux with $\sqrt{\beta_{p,ped}}$ with a coefficient, c_1 , of order 0.1 [9], and for simplicity assigns a coefficient of $c_1 = 0.076$, consistent with a set of observations on DIII-D. EPED1.6, a later version, uses infinite- n proxy calculations, fit to an analytic extension, to calculate c_1 separately for each set of inputs [10]. Both versions find similar levels of agreement with observations. In the following sections we will use the form used in the EPED1 version, which we recall here:

$$\Delta = 0.076\sqrt{\beta_{p,ped}}. \quad (1)$$

Equation (1) will be referred to as the KBM constraint.

Using a minimum number of input parameters (R_0 , a , κ , δ , B_t , I_p , β_N , $n_{e,ped}$, Z_{eff}), a series of model equilibria with varying pedestal width Δ and height p_{ped} are generated. The peeling-ballooning stability curve is computed as the maximum allowable pedestal height for each value of the pedestal width Δ . The intersection of this curve with the one obtained from equation (1) yields the prediction for the pedestal structure (p_{ped} , Δ). This approach has been validated on many different tokamaks obtaining agreement with the experimental values below 15 – 20 % [10]

3. The EPED-CH implementation

3.1. Structure

The basic block for an implementation of the EPED model is the generation of a model equilibria that has a given pedestal height p_{ped} and width Δ and the computation of its stability (only for ideal MHD in the case of the EPED1 version). We will refer to this as a *cell*.

3.1.1. Equilibrium construction As in the original EPED model and consistently with previous studies such as [13], the equilibrium is generated by assuming that the electron temperature T_e and density n_e have a tanh shape in the pedestal region (as a function of the normalized poloidal flux Ψ_N) and a polynomial shape in the core. The ion profiles are computed using $T_i = T_e$ and with a radially flat profile for Z_{eff} for the computation of n_i . The pressure profile is obtained from $p = n_e T_e + n_i T_i$. The parallel current density $I_{\parallel} = \langle \mathbf{J} \cdot \mathbf{B} \rangle / \langle \mathbf{B} \cdot \nabla \phi \rangle$ in the pedestal is dominated by the bootstrap current which is computed using the formulas found in [14, 15]. The core I_{\parallel} profile is polynomial. An example of the profiles obtained for standard parameters

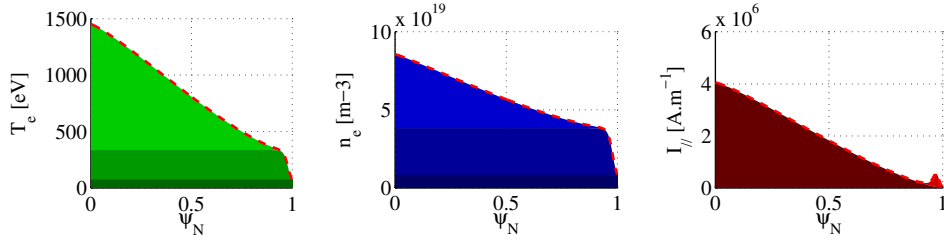


Figure 1. Example of profiles obtained in EPED-CH for T_e (left), n_e (center) and I_{\parallel} (right). For n_e and T_e , the separation between the different colors indicate the value at the separatrix and at the pedestal top.

is shown in figure 1. Finally the shape of the plasma boundary is given by a discrete set of points which can come from analytical formulas, from a simulation or from an experimentally reconstructed equilibrium.

Using all these inputs, the equilibrium is constructed with the CHEASE code [16]. We also use an iterative loop to update the free parameters in our model so as to match the input parameters and to model the pedestal bootstrap current within the required accuracy. Due to the rather complex dependencies between the different input parameters (for example between I_p and the pedestal bootstrap current profile), under-relaxation is often needed to avoid oscillations between iterations. We can also save iterations by providing a good initial guess for all the free parameters (such as the previous (Δ, p_{ped}) cell). The equilibrium construction then takes less than 4 iterations for a 1% accuracy. It is also possible to construct directly an equilibrium where the pedestal profiles satisfy the KBM constraint (1), this can require two more iterations if the average poloidal field at the pedestal top is used.

3.1.2. Stability evaluation In EPED-CH the KBM constraint is computed using equation (1) as in the EPED1 version in lieu of repeating the full BCP calculations used in EPED1.6. Hence only the peeling-ballooning stability of the pedestal needs to be computed. In EPED-CH this is done using the KINX code [17] for a set of chosen toroidal mode numbers: $n = 5, 6, 8, 10, 15, 20, 30, 40$. This set is similar to the one used in the original implementation of the EPED model and is chosen to be representative of the global pedestal stability.

The KINX code is an ideal MHD stability code which uses finite hybrid elements with no poloidal Fourier decomposition in the poloidal direction. This allows a full description of the plasma separatrix including X-points. KINX uses ballooning factor extraction [18] by applying the following formula for transforming the MHD displacement

$$\xi(\psi, \theta, \varphi) = \tilde{\xi}(\psi, \theta) \exp in \left(\varphi - \int_{\theta_0}^{\theta} \nu(\psi, \theta) d\theta \right) \quad (2)$$

where $\nu(\psi, \theta) = \mathbf{B} \cdot \nabla \varphi / \mathbf{B} \cdot \nabla \theta$ is the local field-line pitch and $\tilde{\xi}$ will be the actual unknown function in the eigenvalue problem. This transformation reduces the variation of $\tilde{\xi}$ as a function of θ for flute-like modes where $\mathbf{B} \cdot \nabla \xi \simeq 0$. This helps reducing the necessary grid resolution to achieve the same accuracy for the growthrate and eigenvector and thus saving substantial computing time. Therefore the full ideal model is maintained and solved for both low $n = 1, 2, \dots$ and high n

numbers (up to 100). The code can also be run as a “ δW -code” which can track solutions as they enter the stable region where $\gamma^2 < 0$ and allows to compute stability boundaries more precisely. Figure 2 shows an example of results from the KINX code

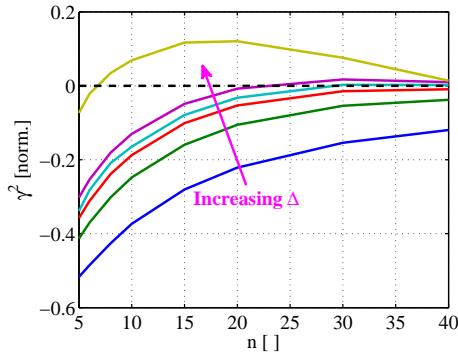


Figure 2. Example of results of the EPED-CH peeling-ballooning stability analysis using KINX. The different curves correspond to different values of the pedestal width Δ with all other parameters kept constant. Here γ^2 means $-\delta W/K$ with negative values corresponding to stable equilibria for the corresponding toroidal mode number n .

for a series of equilibria obtained with the procedure described in the previous section and with increasing pedestal width Δ . Before running KINX, we must generate the appropriate quasi-polar grid of the equilibrium using the Grad-Shafranov solver CAXE [19].

The effect of diamagnetic stabilisation is currently not included in the EPED-CH implementation. However since our study concerns mostly configurations with negative triangularity it is important to note that for these configurations the effect of the diamagnetic stabilisation on the stability boundary is less than for standard positive triangularity configurations [2]. Also it was showed in [20] that in JET ITER-like wall experiments the inclusion of both effects of diamagnetic flows and plasma rotation resulted in peeling-ballooning stability limit for high n modes similar to the one obtained with ideal MHD, these results followed studies for analytical equilibria [21] and JT-60U experiments [22].

3.1.3. Looking for the solution After describing the techniques to construct an equilibrium with a given p_{ped} and Δ and to compute its pedestal stability, we can now move on to describe how the prediction is actually obtained. In the EPED-CH implementation, this can be done in one of two ways.

First we can simply scan the (p_{ped}, Δ) two-dimensional space and compute the pedestal stability for each equilibrium. The solution is then obtained by looking for the intersection of the curves corresponding to the KBM constraint (1) and to the marginal pedestal stability as computed by KINX for all toroidal wavenumbers. This method may take more time to estimate the solution but can also give additional information such as the sensitivity to changes in the two constraints. Note that CPU time can be saved by minimizing the changes in p_{ped} and Δ for the choice of the next cell during the scan, thus providing a good initial guess for the construction of the next equilibrium (see figure 3).

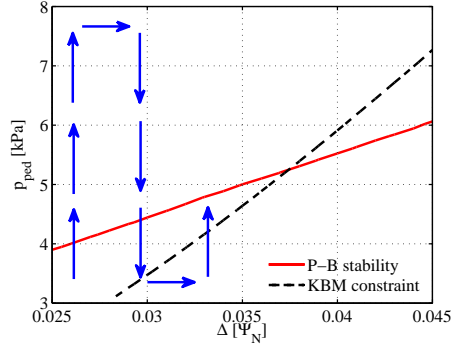


Figure 3. Cartoon illustrating how we can design a path in the (p_{ped}, Δ) plane to minimise changes between successive cells when scanning this 2D space.

Alternatively we can choose the next (p_{ped}, Δ) cell based on the results of the previous cells and their position relative to the two constraints in the model as explained by figure 4. Since for EPED1 p_{ped} is proportional to Δ^2 , we can use a

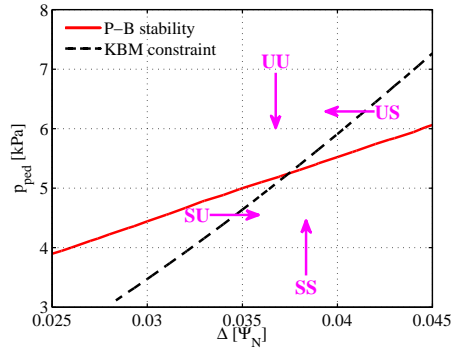


Figure 4. Direction suggested by the search algorithm based on the stability of the current cell. The first letter correspond to the KBM constraint and the second to the peeling-ballooning constraint (with S indicating stability and U instability). In the case where the KBM constraint is equation (1), a simple bisection is used.

simple bisection algorithm where we evolve Δ based on the peeling-ballooning stability of the current equilibrium. Using this method, EPED-CH can obtain a solution with a precision of 0.1 % of the minor radius for Δ in about 6 to 8 iterations. Provided that the stability calculations for all 8 toroidal mode numbers can run in parallel, the required computing (user) time is between 10 and 15 minutes on a standard CPU.

3.2. Comparison with the original EPED results

Before beginning our analysis of the pedestal structure in negative triangularity tokamaks, we compare the results obtained with the present EPED-CH to those obtained and published with the original EPED1 model. We perform two simulations based on two DIII-D discharges. We reproduce in table 1 the list of input parameters for these two discharges found in [23]. We present in figure 5 a comparison between our

DIII-D shot	R_0/m	a/m	κ	δ	B_t/T	I_p/MA	β_N	$n_{e,ped}/10^{19} m^{-3}$
#132003	1.7	0.58	1.8	0.2	1.62	1.16	2.1	5
#132017	1.7	0.59	1.8	0.55	2.1	0.85	2.3	4

Table 1. List of input parameters for the two DIII-D discharges considered (from [23]).

results using EPED-CH and the original EPED1 results. We obtain a good agreement

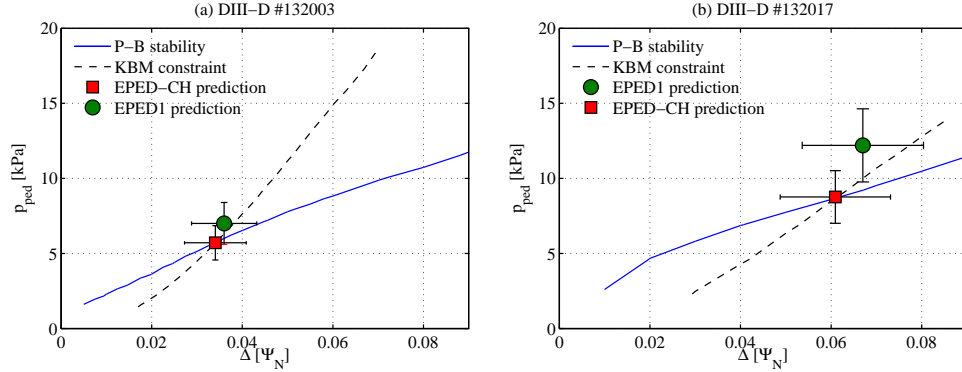


Figure 5. Comparison of the results of two DIII-D discharges using EPED-CH with the original EPED1 results (see figure 5 of [23] where EPED1 is compared with the experimental values). The level of agreement between EPED-CH and EPED1 is comparable to the one of EPED1 with experimental values symbolised by the error bars of 20% [9].

between the two considering the potential differences in the model assumptions, such as for example the specific profile and equilibrium shapes and the absence of the diamagnetic stabilisation effect in EPED-CH. In particular, our EPED-CH simulations are able to reproduce the large difference in pedestal structure between these two cases.

3.3. Comparison with TCV experiments

We continue our testing of EPED-CH by applying it to two similar TCV discharges. The input parameters are shown in table 2, the main difference between these two

TCV shot	R_0/m	a/m	κ	δ	B_t/T	I_p/MA	β_N	$n_{e,ped}/10^{19} m^{-3}$
#38006	0.88	0.22	1.6	0.42	1.4	0.37	1.3	3.6
#37391	0.88	0.22	1.6	0.42	1.4	0.37	0.9	3.4

Table 2. List of input parameters for the two TCV discharges considered. The differences are highlighted in bold.

discharges being that TCV #37391 was purely ohmically heated while TCV #38006 had X2 EC auxiliary heating. This resulted in a larger normalised beta for TCV #38006 and also a slightly larger density at the top of the pedestal. A change in the ELM regime was also observed where TCV #38006 had type-I ELMs whereas TCV #37391 had type-III ELMs.

We show in figure 6 the results of the EPED-CH analysis for these two discharges. The estimate of the experimental value for T_e at the top of the pedestal $T_{e,ped}$

is also shown, we do not show an estimate of the pedestal width Δ due to the relative low number of measurement points inside the pedestal. For the type-I

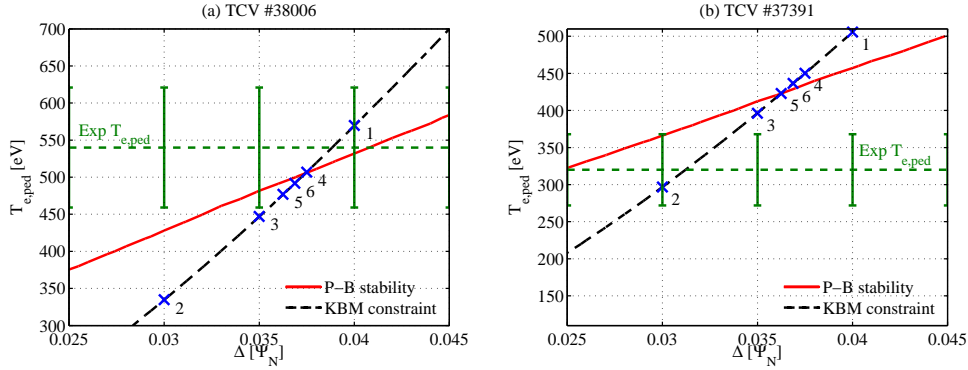


Figure 6. EPED-CH analysis of two TCV discharges. (a) TCV #38006 has type-I ELMy behaviour and EPED-CH recovers well the pedestal height. (b) TCV #37391 has type-III ELMy behaviour and EPED-CH over-estimates the pedestal height by about 100 eV. The parameters for these two discharges can be found in table 2. The blue crosses indicate the successive iterations of EPED-CH when looking for the solution, they are labelled by their iteration number. The error bars for the experimental pedestal height correspond to an uncertainty level of 15 % which is consistent with previous analyses of similar discharges [24].

ELMy discharge TCV #38006, our EPED-CH simulation predicts a temperature at the top of the pedestal of about 500 eV in good agreement with the experimental one at 540 eV. However for type-III ELMy discharge TCV #37391, the simulation largely overestimates the pedestal height predicting a value of 440 eV whereas the experimental value is estimated at 320 eV. The small change in the simulation results between the two discharges can be explained by the proximity of the two sets of input parameters and the relatively small effect of β_N for these weakly-shaped plasmas. Moreover these results with the EPED1 model which aims at predicting the pedestal structure for type-I ELMy discharges are consistent with [24] which found that type-III ELMy discharge are further away from the peeling-ballooning limit. The pedestal width for typical type-I ELMy discharges in TCV is estimated to 8 mm at the plasma mid-plane [24], this corresponds to $\Delta \simeq 0.053$ in units of Ψ_N for the equilibria considered here. This value is in qualitative agreement with our simulation for TCV #38006 which predicts $\Delta \simeq 0.037$.

4. EPED-CH analysis of plasmas with negative triangularity

EPED-CH simulations are able to reproduce with good accuracy both original EPED results and the pedestal structure in type-I ELMy H-mode TCV experiments. We will now focus our analysis on plasmas with negative triangularity.

4.1. Analysis of a TCV upper triangularity scan

We start with a TCV discharge where the upper triangularity (δ_u) was varied from positive to negative values while all other parameters were kept constant (in particular, the lower triangularity was close to 0). We will focus on the two stationary phases

(lasting about 150 ms) at the extreme points in the scan which correspond to $\delta_u = 0.18$ at $t = 0.7$ s and $\delta_u = -0.19$ at $t = 1.8$ s as shown in figure 7. The input parameters for the two simulations are summarised in table 3. The simulation results show a drop in

TCV time	R_0/m	a/m	κ	δ_u	B_t/T	I_p/MA	β_N	$n_{e,ped}/10^{19} m^{-3}$
0.7 s	0.88	0.21	1.7	0.18	1.4	0.30	1.1	2.5
1.8 s	0.88	0.21	1.7	-0.19	1.4	0.28	0.8	2.5

Table 3. List of input parameters for the two time slices of TCV #43872. Note that only the plasma upper triangularity is shown.

$T_{e,ped}$ of about 200 eV for $\delta_u < 0$. This corresponds to a drop in $p_{e,ped}$ of about 40% which is in qualitative agreement with the experimental drop of 20% found in [4]. Figure 7 also shows the EPED-CH predicted profiles compared with the experimental measurements from Thomson Scattering [25, 26]. Again in this case, it was not possible

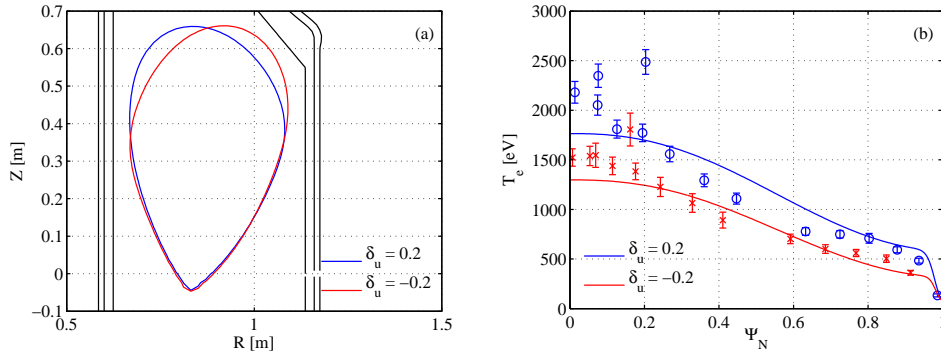


Figure 7. (a) Boundary shapes for TCV discharge #43872 with the positive δ_u in red and the negative δ_u in blue. (b) Electron temperature profiles predicted by EPED-CH as solid lines compared to the Thomson Scattering measurements as circles with error bars, the same color coding as (a) applies. A single TS pulse is shown for both triangularities. EPED-CH recovers the qualitative experimental result with a drop of $T_{e,ped}$ of about 200 eV.

to estimate the pedestal width Δ from the experimental measurements, however the predicted value $\Delta = 0.035$ is still in qualitative agreement with the values found in [24]. It is important to note that this drop in pedestal height is only due to a change in the plasma upper triangularity and resulting pedestal stability, all other parameters including the line-averaged and pedestal top electron density remained constant during the scan except for an increase of the EC X2 power. The stiff nature of the core transport explains the concurrent drop in β_N (despite the increase in X2 power) and we do not expect a large effect of this drop in β_N on the pedestal stability in return, as will be discussed below.

4.2. Predictions for the Negative Triangularity Tokamak

The Negative Triangularity Tokamak (NTT) concept considered here is a large conceptual machine with the following parameters $R_0 = 9$ m, $a = 3$ m, $B_0 = 5$ T, $I_p = 15$ MA. It has an elongation of $\kappa = 1.8$, a lower single-null configuration with the X-point close to the outer wall with a lower triangularity of $\delta_l = -0.85$. It was

shown that this configuration can be stable up to $\beta_N \simeq 3$ with high ($\delta_u = -0.5$) or low ($\delta_u = 0$) upper triangularity [1, 2].

We assume that the pedestal density is close to the Greenwald density which for these parameters means $n_{e,ped} \simeq 5 \times 10^{19} \text{ m}^{-3}$ and that the peaking factor $n_{e,0}/n_{e,ped}$ (where $n_{e,0}$ is the central density) is 1.5 which is close to the value predicted for ITER. In terms of the normalised density gradient, this means $R/L_{n_e} \simeq 1$. For comparison purposes we will also consider a case where the shape is flipped around the $R = R_0$ axis such as to obtain a standard Positive Triangularity Tokamak (or PTT) and all other parameters are kept constant. Unless stated otherwise the case with low ($\delta_u = 0$) upper triangularity will be considered.

4.2.1. Pedestal structure Our EPED-CH simulation for the NTT case yields the following prediction for the pedestal top pressure $p_{ped} = 9.2 \text{ kPa}$ and pedestal top electron temperature $T_{e,ped} = 640 \text{ eV}$. If we now switch to the PTT case, we obtain $p_{ped} = 39 \text{ kPa}$, $T_{e,ped} = 2.7 \text{ keV}$. In figure 8 we show the detailed dependence of the

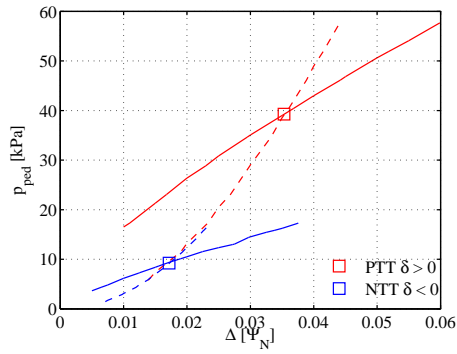


Figure 8. Results of the EPED-CH analysis. The solid line indicates the peeling-ballooning stability boundary, the dashed line the KBM constraint given by equation (1) and the square marks the position of the EPED-CH prediction. The blue items correspond to the NTT basic parameters, the red ones to the PTT case where the shape is flipped around $R = R_0$.

constraints in both cases. First the shape of the curve representing the KBM constraint is mostly unchanged due to the fact that in this case the relationship between p_{ped} and Δ only involve I_p and the perimeter of the plasma boundary, which are unchanged between both cases. For the peeling-ballooning stability constraint, the maximum pedestal height for the NTT case is smaller by a factor of two for a given pedestal width. The coupling of the two constraints in the EPED1 model yields an even bigger reduction as p_{ped} is reduced by a factor 4 as compared to the PTT case.

As the volume increase between positive and negative triangularity is very moderate, only increasing by 5% for NTT compared to PTT, the change for $W_{ped} = (3/2)p_{ped}V$ is also of a factor of 4 going from 39.1 MJ for NTT to 157 MJ for PTT. This strong reduction in the pedestal stored energy should translate in a strong reduction of the ELM losses if $\Delta W_{ELM}/W_{ped}$ is similar in both cases, as has been observed in TCV ELMy H-modes with negative triangularity. We would like to stress the fact that the PTT case is not optimised with respect to the pedestal height: as can be seen in figure 10 of section 4.2.4 pedestal heights of 80 kPa (more than 8 times larger

than the standard NTT case) can be obtained by only varying the top and bottom triangularities.

4.2.2. Core performance A smaller pedestal is beneficial regarding power handling but this should not be at the cost of the overall performance. While, strictly speaking, the EPED1 model does not predict profiles in the core, it does include nominal core profiles which match the input β_N , and can be used as a starting point to investigate core physics. In our simulation for the NTT base case, good core performance was achieved with a central T_e of about 40 keV. Since the central temperature is a result of our choice of β_N close to the global stability limit (2.9 in our case [2]) and density peaking factor, we need to check the normalised temperature gradient values in order to assess the plausibility of such central value. If we take the average of R/L_{T_e} between the sawtooth inversion radius ($\rho_{tor,norm} = 0.3$) and the pedestal top ($\rho_{tor,norm} = 0.95$) we obtain a value of 14. This value can even be lowered in our simulations if we assume $n_{ped} > n_{GW}$ or if we consider a larger density peaking factor. Nevertheless, this value is still compatible with the present understanding of core turbulence. For example, in [27] it is shown that for dominant electron heating discharges and in a broad range of tokamaks the value of R/L_{T_e} at mid-radius is in the range of 8 to 12. In section 3.3.1 of [28] it is stated that with dominant electron heating the experimental values of R/L_{T_e} can exceed the turbulent threshold value (typically in the range of 3 to 5) by a factor of 2 to 3. Another figure of merit for the core profile peaking is the ratio of the volume-averaged pressure to the pedestal pressure $\langle p \rangle_V / p_{ped}$, its value reaches around 30 for our NTT base case, well above the PTT case at 7.5 and experimental values both on TCV and other tokamaks typically around 2 to 4. The feasibility of such values both for R/L_{T_e} and $\langle p \rangle_V / p_{ped}$ will have to be confirmed using first principles transport simulations.

4.2.3. Comparing positive and negative triangularity In order to better understand the difference in the peeling ballooning stability for positive and negative triangularity, we will analyse the predicted equilibria using standard pedestal stability analysis. This standard analysis consists in generating a series of equilibria by scaling p' and $I_{||}$ independently in the pedestal region keeping a fixed pedestal width Δ and then computing the finite- n peeling-ballooning stability boundary using KINX and the local infinite- n ballooning stability boundary [29] at each magnetic surface inside the pedestal region.

In the case of positive triangularity there exists a second stability region for local ballooning modes which are stable at high pedestal current (or low magnetic shear) and high pressure gradient. The stability of medium to high n mode numbers follows the same trend while the low n modes are unstable for large pedestal current. If we look at the stability diagram in figure 9(a) we obtain the well-known “nose” shape where a path to large pressure gradients is open by increasing the current density in the pedestal.

As shown in [2] and in figure 9(b), for negative triangularity, the second stability region for ballooning modes is absent and the nose disappears, preventing access to the high pressure gradient region. Instead all mode numbers share essentially the same stability boundary where the maximum stable pressure gradient decreases with increasing pedestal current density.

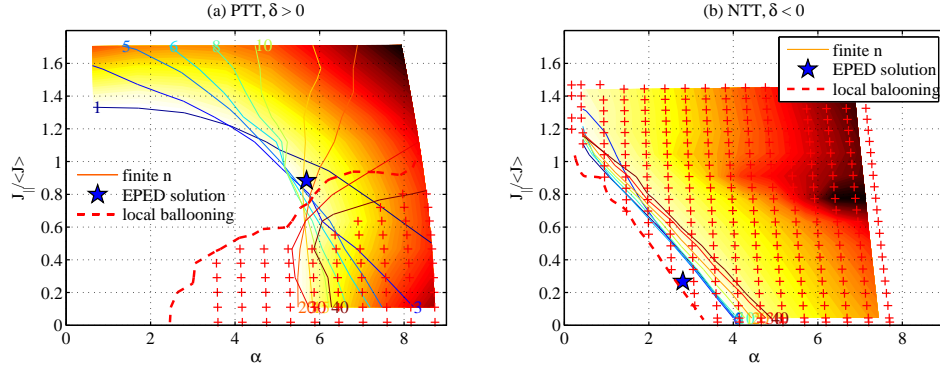


Figure 9. Comparison of the pedestal stability diagram for positive (a) and negative (b) triangularity. The thick solid color lines indicate the stability boundaries for the different toroidal mode numbers. The maximum growth rate is shown as a contour plot (darker colours indicate larger growth rate). Red crosses correspond to equilibria whose pedestals are unstable for local infinite- n ballooning modes (the same representation was used previously in [2, 18]), the dashed red curve separates these equilibria from those that are completely stable for local infinite- n ballooning modes. For this figure the case with high upper triangularity ($|\delta_u| = 0.5$) was used as reference, the full list of parameters can be found in section 4.2.

4.2.4. *Sensitivity to triangularity* We now perform some sensitivity studies for our EPED-CH prediction.

As a first study we vary independently the upper and lower triangularity of the plasma by using equations (A.1) and (A.2) as the prescribed boundary. The results are presented in figure 10 and they show that p_{ped} (and Δ) increase when going from negative to positive triangularity. The pedestal height is seen to depend mostly on

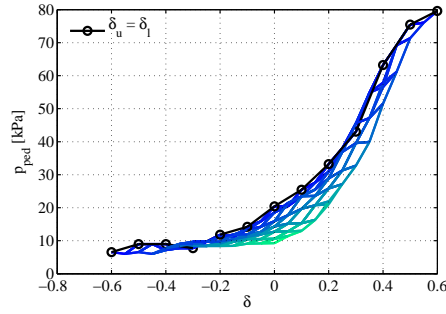


Figure 10. Projection of the results of the two-dimensional scan in (δ_u, δ_l) (other parameters are kept fixed). The pedestal height p_{ped} is plotted against the mean triangularity $\delta = (\delta_u + \delta_l)/2$. Black circles indicate up-down symmetric equilibria where $\delta_u = \delta_l$. The color indicates deviation from up-down symmetry going from blue to green for more asymmetry.

the average triangularity $\delta = (\delta_u + \delta_l)/2$. But at constant δ , the highest pedestals are obtained when the plasma is up-down symmetric with $\delta_u = \delta_l$. Another important result is that below a value of $\delta = -0.2$, the pedestal height is almost independent of the choice of upper and lower triangularity. Therefore our results obtained for the

low upper triangularity design ($\delta_u = 0$) remain true for the large upper triangularity design ($\delta_u = -0.5$).

4.2.5. Sensitivity to the pedestal density If we now vary the density at the top of the pedestal, we see that the pedestal pressure increases with increasing pedestal density although the pedestal temperature decreases. We performed the same scan in the case

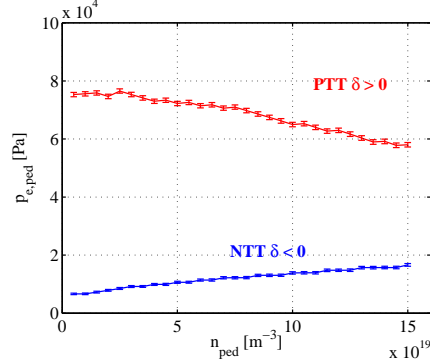


Figure 11. Pedestal height p_{ped} as a function of the pedestal density $n_{e,ped}$ for two $n_{e,ped}$ scans based on the NTT (blue) and PTT (red) cases (other parameters are kept fixed). The overall trend is reversed for the two cases. The case with high upper triangularity ($|\delta_u| = 0.5$) was used as reference, the full list of parameters can be found in section 4.2. For the PTT case with low upper triangularity, the pedestal height first increases with pedestal density before decreasing for $n_{e,ped} > 8 \times 10^{19} \text{ m}^{-3}$.

of positive triangularity and we can see in figure 11 that the global trend is reversed. This can be explained in light of the stability diagrams: both simulations lie in the range of parameters where the increase of the density, and thus of the collisionality in the pedestal, causes a decrease of the bootstrap current density. This means that the solutions will have to move down in the (J_{\parallel}, α) diagram and the variation in α will result from the particular shape of the stability boundary (see the magenta arrows in figure 12). For positive triangularity the solution moves to lower values of α (and thus lower pedestal height) while for negative triangularity the solution moves to larger α values.

Note that for both $n_{e,ped}$ scans the case with high upper triangularity ($|\delta_u| = 0.5$) was used. For low upper triangularity, the only difference concerns the positive triangularity. In this case the EPED prediction is not at the tip of the “nose” in the (J_{\parallel}, α) diagram but rather on its upper boundary, and when $n_{e,ped}$ increases the solution first moves towards the tip of the nose, meaning higher α , p_{ped} values before coming down the lower boundary towards lower α , p_{ped} values.

4.2.6. Sensitivity to the core pressure Finally we investigate the effect of increasing the global β_N on the pedestal structure in figure 13. For positive triangularity we observe a large increase of the pedestal height with increasing β_N . This is a well-known effect [30, 31] which is linked to an easier access to the second stability region for ballooning modes and where the nose in the stability diagram gets longer. However, due to the closed access to the second stability region for negative triangularity, the

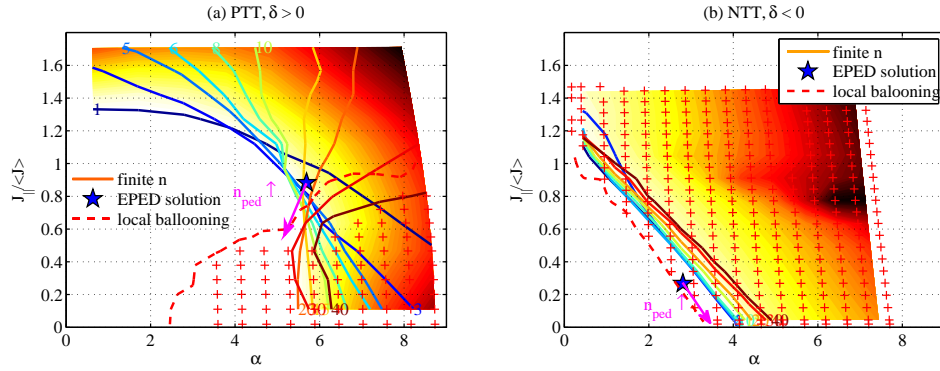


Figure 12. Repetition of figure 9 where we now indicate the trend when the pedestal density is increased. In both cases the pedestal current density decreases, leading in a decrease of α for the PTT case and an increase of α for the NTT case.

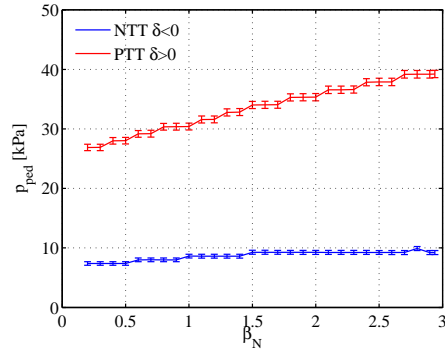


Figure 13. Evolution of the pedestal height p_{ped} when the global normalised beta β_N is increased for the negative (blue) and positive (red) triangularity case (other parameters are kept fixed). The full list of parameters can be found in section 4.2. For positive triangularity the stability is improved allowing for higher pedestals but also higher ELM losses, while for negative triangularity the effect is much smaller.

pedestal height is only weakly increasing with β_N for the NTT base case. Following our initial assumption this means that going to high β_N will be less detrimental regarding ELM power loads on the divertor for NTT compared to PTT. One important caveat in the case of NTT is the fact that as p_{ped} is almost not increasing with β_N , the gradient scale-lengths in the core will increase significantly with increasing β_N and the plausibility of such peaked profiles will have to be investigated.

5. Conclusion

We have presented in this paper a new implementation of the EPED model called EPED-CH which uses the SPC codes CHEASE / CAXE / KINX. At this stage, It uses a simple analytic expression for the KBM constraint as in the EPED1 version. It also does not include any diamagnetic stabilisation for peeling-ballooning modes which

has little effect on the stability boundary for negative triangularity configurations. The results of EPED-CH compare well with the original EPED results. A first comparison with TCV experiments showed good agreement for Type-I ELMy discharges and also recovers the basic dependence of the pedestal height p_{ped} on the plasma upper triangularity observed in TCV ELMy H-modes..

Simulations with EPED-CH show that the predicted pedestal height for the Negative Triangularity Tokamak concept is smaller by a factor of 4 as compared to the standard positive triangularity configuration. This can potentially reduce the peak heat flux due to ELMs while still being compatible with high performance with $\beta_N \simeq 2.9$, central $T_e \simeq 40$ keV and $R/L_T \simeq 14$. It also makes impossible any single large ELM event. Sensitivity studies have shown that p_{ped} depends most strongly on the average triangularity δ and increases when δ goes from negative to positive values. For $\delta \leq -0.2$ the solution is almost insensitive to δ . In contrast with standard $\delta > 0$ configurations, p_{ped} scales favourably with $n_{e,ped}$ and increases only weakly with β_N .

To confirm and improve the quality of these predictions, certain aspects could be investigated. While the EPED KBM constraint has been found to vary only weakly with triangularity, the calculations were performed so far only with zero or positive triangularity. It would be interesting to explore possible variations at negative triangularity. One way would be to develop the BCP technique described in [10] and used in EPED1.6 for negative triangularity plasmas. One critical point will be to assess the compatibility of a low pedestal with the good core performance needed in a device such as a demonstration power plant. This could be investigated using first-principles transport simulations. This could prove a challenging task in view of the relatively high values for R/L_T or $\langle p \rangle_V / p_{ped}$. This study could also be coupled with the ongoing effort of modelling the NTT concept with system codes [32]. Finally the link between reduced pedestal height, reduced ELM losses and reduced peak heat flux for $\delta < 0$ could be addressed using non-linear MHD simulations.

Acknowledgements

The work was partly supported by the grant from the Russian Science Foundation #16-11-10278 and by the Competitiveness Programme of NRNU MEPhI and by the Swiss National Science Foundation.

References

- [1] M Kikuchi, S Medvedev, T Takizuka, A Fasoli, Y Wu, P Diamond, X Duan, A Ivanov, A Martynov, Y Poshekhonov, Y Ueda, L Yan, X Song, and G Zheng. Perspective of Negative Triangularity Tokamak as Fusion Energy System. In *42nd EPS Conference on Plasma Physics and Controlled Fusion*, volume ECA Vol. 3, page P4.179, Lisbon, Portugal, 2015.
- [2] S.Yu. Medvedev, M. Kikuchi, L. Villard, T. Takizuka, P. Diamond, H. Zushi, K. Nagasaki, X. Duan, Y. Wu, A.A. Ivanov, A.A. Martynov, Yu.Yu. Poshekhonov, A. Fasoli, and O. Sauter. The negative triangularity tokamak: stability limits and prospects as a fusion energy system. *Nuclear Fusion*, 55(6):063013, 2015.
- [3] Y. Camenen, A. Pochelon, R. Behn, A. Bottino, A. Bortolon, S. Coda, A. Karpushov, O. Sauter, G. Zhuang, and the TCV Team. Impact of plasma triangularity and collisionality on electron heat transport in TCV L-mode plasmas. *Nuclear Fusion*, 47:510–516, 2007.
- [4] A. Pochelon, P. Angelino, R. Behn, S. Brunner, S. Coda, N. Kirneva, S. Yu Medvedev, H. Reirmerdes, J. Rossel, O. Sauter, L. Villard, D. Wagner, A. Bottino, Y. Camenen, G. P. Canal, P. K. Chattopadhyay, B. P. Duval, A. Fasoli, T. P. Goodman, S. Jolliet, A. Karpushov, B. Labit, A. Marinoni, J. Moret, A. Pitzschke, L. Porte, M. Rancic, V. S. Udintsev, and the

- TCV Team. Recent TCV Results - Innovative Plasma Shaping to Improve Plasma Properties and Insight. *Plasma and Fusion Research*, 7(SPL.ISS.1):2502148–2502148, 2012.
- [5] S Yu Medvedev, A A Ivanov, A A Martynov, Yu Yu Poshekhonov, R Behn, Y R Martin, A Pochelon, O Sauter, and L Villard. Beta Limits and Edge Stability for Negative Triangularity Plasmas in the TCV Tokamak. In *35th EPS Conference on Plasma Phys. Hersonissos, 9 - 13 June 2008*, volume ECA Vol.32, pages P–1.072, Hersonissos, 2008.
- [6] Fabio Riva, Emmanuel Lanti, Sébastien Jolliet, and Paolo Ricci. Plasma shaping effects on tokamak scrape-off layer turbulence. *Plasma Physics and Controlled Fusion*, 59(3):035001, 2017.
- [7] A W Leonard. Edge-localized-modes in tokamaks. *Physics of Plasmas*, 21(9):090501, 2014.
- [8] H. Thomsen, T. Eich, S. Devaux, G. Arnoux, S. Brezinsek, E. DelaLuna, W. Fundamenski, A. Herrmann, A. Huber, S. Jachmich, P. Lomas, I. Nunes, G. Saibene, A. Scarabosio, and J. Schweinzer. Power load characterization for type-I ELMy H-modes in JET. *Nuclear Fusion*, 51(12):123001, 2011.
- [9] P. B. Snyder, R. J. Groebner, A. W. Leonard, T. H. Osborne, and H. R. Wilson. Development and validation of a predictive model for the pedestal height. *Physics of Plasmas*, 16(5):056118, 2009.
- [10] P. B. Snyder, R. J. Groebner, J. W. Hughes, T. H. Osborne, M. Beurskens, A. W. Leonard, H. R. Wilson, and X. Q. Xu. A first-principles predictive model of the pedestal height and width: development, testing and ITER optimization with the EPED model. *Nuclear Fusion*, 51(10):103016, 2011.
- [11] P. B. Snyder, T. H. Osborne, K. H. Burrell, R. J. Groebner, a. W. Leonard, R. Nazikian, D. M. Orlov, O. Schmitz, M. R. Wade, and H. R. Wilson. The EPED pedestal model and edge localized mode-suppressed regimes: Studies of quiescent H-mode and development of a model for edge localized mode suppression via resonant magnetic perturbations. *Physics of Plasmas*, 19(5):056115, 2012.
- [12] P. B. Snyder and H. R. Wilson. Ideal magnetohydrodynamic constraints on the pedestal temperature in tokamaks. *Plasma Physics and Controlled Fusion*, 45(9):1671–1687, 2003.
- [13] P. B. Snyder, H. R. Wilson, T. H. Osborne, and A. W. Leonard. Characterization of peeling–ballooning stability limits on the pedestal. *Plasma Physics and Controlled Fusion*, 46(5A):A131–A141, 2004.
- [14] O Sauter, Clemente Angioni, and Y R Lin-Liu. Neoclassical conductivity and bootstrap current formulas for general axisymmetric equilibria and arbitrary collisionality regime. *Physics of Plasmas*, 6(7):2834, 1999.
- [15] O. Sauter, C. Angioni, and Y. R. Lin-Liu. Erratum: "Neoclassical conductivity and bootstrap current formulas for general axisymmetric equilibria and arbitrary collisionality regime" [Phys. Plasmas 6, 2834 (1999)]. *Physics of Plasmas*, 9(12):5140, 2002.
- [16] H. Lütjens, A. Bondeson, and O. Sauter. The CHEASE code for toroidal MHD equilibria. *Computer Physics Communications*, 97(3):219–260, 1996.
- [17] L. Degtyarev, A. Martynov, S. Medvedev, F. Troyon, L. Villard, and R. Gruber. The KINX ideal MHD stability code for axisymmetric plasmas with separatrix. *Computer Physics Communications*, 103(1):10–27, 1997.
- [18] S Yu Medvedev, A A Martynov, Y R Martin, O Sauter, and L Villard. Edge kink/ballooning mode stability in tokamaks with separatrix. *Plasma Physics and Controlled Fusion*, 48(7):927–938, 2006.
- [19] S. Medvedev, L. Villard, L. M. Degtyarev, A. Martynov, R. Gruber, and F. Troyon. MHD equilibrium and stability of doublet configurations. In *Proc. 20th EPS Conference on Controlled Fusion and Plasma Physics, vol. 17C*, pages 1279–1282, Lisboa, Portugal, 1993.
- [20] N. Aiba, C. Giroud, M. Honda, E. Delabie, S. Saarelma, L. Frassinetti, I. Lupelli, S. Pamela, H. Urano, C.F. Maggi, and JET Contributors. Numerical analysis of ELM stability with rotation and ion diamagnetic drift effects in JET. *Nuclear Fusion*, 2017.
- [21] N. Aiba. Impact of ion diamagnetic drift on ideal ballooning mode stability in rotating tokamak plasmas. *Plasma Physics and Controlled Fusion*, 58(4):045020, 2016.
- [22] N. Aiba, M. Honda, and K. Kamiya. Impact of ion diamagnetic drift on MHD stability at edge pedestal in JT-60U rotating plasmas. *Nuclear Fusion*, 57(2):022011, 2017.
- [23] P. B. Snyder, N. Aiba, M. Beurskens, R. J. Groebner, L. D. Horton, A. E. Hubbard, J. W. Hughes, G. T. A. Huysmans, Y. Kamada, A. Kirk, C. Konz, A. W. Leonard, J. Lönnroth, C. F. Maggi, R. Maingi, T. H. Osborne, N. Oyama, A. Pankin, S. Saarelma, G. Saibene, J. L. Terry, H. Urano, and H. R. Wilson. Pedestal stability comparison and ITER pedestal prediction. *Nuclear Fusion*, 49(8):085035, 2009.
- [24] A Pitzschke, R Behn, O Sauter, B P Duval, J Marki, L Porte, L Villard, and S Yu Medvedev.

- Electron temperature and density profile evolution during the edge-localized mode cycle in ohmic and electron cyclotron-heated H-mode plasmas in TCV. *Plasma Physics and Controlled Fusion*, 54(1):015007, 2012.
- [25] R Behn, S Franke, Z.A. Pietrzyk, M. Anton, Chr. Nieswand, H. Weisen, and B. Marletaz. The Thomson scattering diagnostic on TCV. In *7th International Symposium on "Laser-Aided Plasma Diagnostics"*, pages 392–7, Fukuoka, Japan, 1995.
- [26] Andreas Pitzschke. *Pedestal Characteristics and MHD Stability of H-Mode Plasmas in TCV*. PhD thesis, École Polytechnique Fédérale de Lausanne, EPFL, 2011.
- [27] F Ryter, C Angioni, M Beurskens, S Cirant, G T Hoang, G M D Hogeweij, F Imbeaux, A Jacchia, P Mantica, W Suttrop, and G Tardini. Experimental studies of electron transport. *Plasma Physics and Controlled Fusion*, 43(12A):A323–A338, 2001.
- [28] E. J. Doyle, W. A. Houlberg, Y. Kamada, V. Mukhovatov, T. H. Osborne, A. Polevoi, G. Bateman, J. W. Connor, J. G. Cordey, T. Fujita, X. Garbet, T. S. Hahm, L. D. Horton, A. E. Hubbard, F. Imbeaux, F. Jenko, J. E. Kinsey, Y. Kishimoto, J. Li, T. C. Luce, Y. Martin, M. Ossipenko, V. Parail, A. Peeters, T. L. Rhodes, J. E. Rice, C. M. Roach, V. Rozhansky, F. Ryter, G. Saibene, R. Sartori, A. C. C. Sips, J. A. Snipes, M. Sugihara, E. J. Synakowski, H. Takenaga, T. Takizuka, K. Thomsen, M. R. Wade, H. R. Wilson, ITPA Transport Physics Topical Group, ITPA Confinement Database and Modelling Topical Group, and ITPA Pedestal and Edge Topical Group. Chapter 2: Plasma confinement and transport. *Nuclear Fusion*, 47(6):S18, 2007.
- [29] J W Connor, R J Hastie, and J B Taylor. Shear, Periodicity, and Plasma Ballooning Modes. *Physical Review Letters*, 40(6):396–399, 1978.
- [30] P. B. Snyder, K. H. Burrell, H. R. Wilson, M. S. Chu, M. E. Fenstermacher, a. W. Leonard, R. a. Moyer, T. H. Osborne, M. Umansky, W. P. West, and X. Q. Xu. Stability and dynamics of the edge pedestal in the low collisionality regime: physics mechanisms for steady-state ELM-free operation. *Nuclear Fusion*, 47(5):961–968, 2007.
- [31] I T Chapman, A Merle, S Saarelma, R Cesario, S Coda, J W Connor, E de la Luna, R Fisher, L Garzotti, C J Ham, R J Hastie, J Hobirk, A Kirk, C F Maggi, O McCormack, O Sauter, R Scannell, J Simpson, E Solano, H Urano, W Wright, JET Contributors, the MAST Team, the TCV Team, and the EUROfusion MST1 Team. Joint experiments tailoring the plasma evolution to maximise pedestal performance. In *Proc. 26th IAEA Fusion Energy Conference*, pages EX/3–6, Kyoto, Japan, 2016.
- [32] S.Yu. Medvedev, M. Kikuchi, T. Takizuka, A.A. Ivanov, A.A. Martynov, Yu.Yu. Poshekhonov, A. Merle, O. Sauter, L. Villard, D. Chen, J. Jiang, J.X. Li, J. Zheng, and T. Ando. Single Null Divertor in Negative Triangularity Tokamak. In *FEC 2016 Kyoto*, pages ICC/P3–47, 2016.

Appendix A. Analytical boundary with different upper and lower triangularity

We use the following formulas for prescribing the shape of the plasma separatrix.

$$R(\theta) = R_0 + \begin{cases} a \cos(\theta + (\arcsin \delta_u) \sin \theta) & \text{if } 0 \leq \theta \leq \pi \\ a \cos(\theta + (\arcsin \delta_l) \sin \theta) & \text{if } \pi \leq \theta \leq 2\pi \end{cases} \quad (\text{A.1})$$

$$Z(\theta) = Z_0 + \kappa a \sin \theta \quad (\text{A.2})$$

where R_0 and Z_0 are the radial and vertical position of the geometric center of the separatrix, a is the minor radius, κ is the elongation and δ_u (δ_l) is the upper (lower) triangularity.

The form of equations (A.1,A.2) guarantee that δ_u matches the standard definition for the top triangularity of the plasma boundary $\delta_u = (R_o + R_i - 2R_t)/(R_o - R_i)$ where R_t , R_o and R_i are the major radii at the topmost, outermost and innermost points of the plasma boundary. This holds as long as the innermost and outermost points correspond to $\theta = \pi$ and $\theta = 0$, i.e. $|\arcsin \delta_{u,l}| \leq 1$ or $|\delta_{u,l}| \leq 0.8415$. In [16] the arcsin function is dropped in equations (A.1,A.2) and therefore the correspondence between δ_u and top triangularity is only valid at low δ_u values.